

Thermodynamics of Lithium Stripping and Limits for Fast Discharge in Lithium Metal Batteries

Victor Venturi[†] and Venkatasubramanian Viswanathan^{*,†,‡}

[†]*Department of Mechanical Engineering, Carnegie Mellon University, Pittsburgh, Pennsylvania 15213, USA*

[‡]*Department of Physics, Carnegie Mellon University, Pittsburgh, Pennsylvania 15213, USA*

E-mail: venkvis@cmu.edu

Abstract

Lithium metal batteries are seen as a critical piece towards electrifying aviation. During charging, plating of lithium metal, a critical failure mechanism, has been studied and mitigation strategies have been proposed. For electric aircraft, high discharge power requirements necessitate stripping of lithium metal in an uniform way and recent studies have identified the evolution of surface voids and pits as a potential failure mechanism. In this work, using density functional theory calculations and thermodynamic analysis, we investigate the discharge process on lithium metal surfaces. In particular, we calculate the tendency for vacancy congregation on lithium metal surfaces, which constitutes the first step in the formation of voids and pits. We find that among the low Miller index surfaces, the (111) surface is the least likely to exhibit pitting issues. Our analysis suggests the faceting control during electrodeposition could be a key pathway towards simultaneously enabling both fast charge and fast discharge.

Lithium-ion batteries are now widely used for portable electronic devices and electric vehicles due to their large voltage window, high energy density, and versatility, among other advantageous characteristics.¹⁻³ Electrification of long-haul trucks,⁴ vertical take-off and landing (eVTOL) aircraft,⁵ and regional and narrow-body aircraft,^{6,7} requires higher specific energy than possible with current Li-ion batteries. Lithium metal anodes are seen as a critical enabler towards meeting these targets,^{3,8,9} but technical hurdles remain hindering their commercialization.

Much of said issues stem from the myriad of processes that can take place at interfaces between different materials, but especially at the anode surface.¹⁰⁻¹⁴ During charging of the lithium metal battery, formation and growth of dendrites in the plating process has been widely-studied and identified as a critical failure mechanism and mitigation strategies have been proposed.^{9,15-23} Electric aircraft applications, in particular, eVTOL, require high discharge power, which can cause new failure mechanisms during the lithium stripping process.²⁴⁻²⁸ Since the morphology of the surface of the lithium anode post-discharge can heavily impact the deposition process in subsequent cycles,²⁹⁻³¹ it is critical to develop a fundamental understanding of void and pit formation associated with lithium stripping.

One of the earliest stages in the formation of these voids is the congregation of vacancies on the lithium surface. In order to understand this mechanism, we use a regular solution model to simulate the anode surface as a mixture of vacancies and lithium atoms, which are treated as two separate particles. The Gibbs free energy of mixing, normalized by the total number of particles, is given by

$$\Delta g_{mix} = \frac{z}{2} x_V x_L (2\epsilon_{VL} - \epsilon_{VV} - \epsilon_{LL}) + k_B T [x_V \log(x_V) + x_L \log(x_L)], \quad (1)$$

where z is the coordination number of the two species, k_B is Boltzmann's constant, T is the system temperature, x_V and x_L are the fraction of particles that are vacancies and lithium atoms, respectively (such that $x_V + x_L = 1$), and the ϵ_{ij} terms are the interaction energies

between species. According to this model, a phase transition occurs at a temperature

$$T_c = \frac{\Omega}{2k_B}, \quad (2)$$

where $\Omega = (z/2)(2\epsilon_{VL} - \epsilon_{VV} - \epsilon_{LL})$. At temperatures higher than T_c , the vacancies are fully soluble in the mixture, and, at lower temperatures, two phases coexist: one with high concentration while the other with a low concentration of vacancies. In this formalism, a high vacancy phase corresponds to the onset of void formation.

Using density functional theory calculations, we analyze this model for three low Miller index lithium surface facets: (100), (110), and (111). A schematic of the different surface interactions considered is shown in Figure 1. For each facet, we examined two possible interactions: one between vacancies which are both located on the same Miller plane on the surface (shown in purple), and another between vacancies that are located on different Miller planes, where one is at the surface, and another is right below it (shown in orange). For simplicity, we will use superscripts 1 and 2 to denote the surface-level Miller plane and the plane immediately under it, respectively. For example, $\Omega^{(11)}$ denotes the interaction parameter on the surface plane (intra-plane), while $\Omega^{(12)}$ corresponds to the interaction parameter between the two different Miller planes mentioned (inter-plane). Note that, for the (110) facet, further distinctions have to be made: there are two different intra-plane interactions, one with four neighbors, and one with two neighbors, as well as two different inter-plane interactions, both with only two neighbors, as represented in Figure 1. Due to the limitations of the regular solution model, it is infeasible to take into account all these different possibilities separately. Therefore, in the case of the (110) surface, we incorporate these distinct interactions by averaging them together, in proportion to the number of neighbors involved.

We used density functional theory (DFT), coupled with the Perdew, Burke, and Ernzerhof (PBE) exchange correlation functional³² in the projector augmented wave (PAW) code

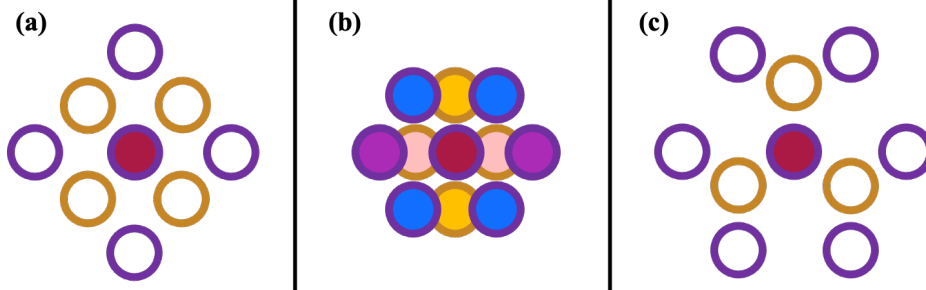


Figure 1: Top-view schematic of the different possible interactions considered for the (a) (100), (b) (110), and (c) (111) lithium surface facets. Purple circles denote lattice sites on the outer-most surface layer, and yellow orange circles denote sites on the second outer-most layer. In the (110) case (panel (b)), there are several different pair-wise interactions: red-purple, red-blue, red-yellow, and red-pink. In the other two cases, all purple-purple and orange-orange site interactions are equivalent.

GPAW³³ implemented in the Atomic Simulation Environment (ASE),³⁴ to calculate the different interaction parameters. Computational details can be found in the Supplementary Information. The results of our analysis are summarized in Table 1, which also includes the average distances, denoted by $d^{(11)}$ and $d^{(12)}$, between a lithium atom in the surface-level Miller plane and a neighboring lattice site, in either the same plane or in the one below. The Brillouin zone was sampled using the Monkhorst Pack scheme.

Our estimates indicate that all three facets have similar surface energy and hence, could all be formed during the electrodeposition process. Controlling the facet has been demonstrated in the context of lithium electrodeposition.³⁵ Vacancy-vacancy interactions are highly favorable in the (100) facet, regardless of the Miller planes of the vacancies, but their attraction is stronger when they are both on the top plane. This implies that the critical temperature for vacancy solubility in this surface is extremely high, above 1300 K, and that, under equilibrium conditions, vacancies will tend to phase separate and, thus, initiate the formation of large voids. Similar to the (100) facet, the strongest interactions in the (110) facet are also intra-plane; however, in this case, the inter-plane interactions are much weaker, and entropic contributions push vacancies in different planes apart even at low temperatures. Therefore, in this case, vacancies are expected to congregate on the top Miller plane, and, in doing so, form steps on the surface, which leads to increased surface roughness and facil-

Table 1: Approximate surface energies, coordination numbers, interaction parameters, and critical temperatures for different surface facets. Given the relatively small difference in surface energies, it is fair to assume all facets are equally relevant. The strongest interactions in the (100) and (110) facets have very high critical temperatures for vacancy solubility (above 1000 K), meaning that, under standard operating conditions, vacancies will tend to phase separate and begin forming voids. That is not the case for the (111) surface, where vacancies are fully solvable and, under equilibrium conditions, should be uniformly distributed on the surface.

Facet	(100)	(110)	(111)
$z^{(11)}$	4	6	6
$z^{(12)}$	4	4	3
γ [eV/Å ²]	~ 0.030	~ 0.031	~ 0.034
$\langle d^{(11)} \rangle$ [Å]	3.44	3.13	4.86
$\langle d^{(12)} \rangle$ [Å]	3.03	3.17	3.05
$\Omega^{(11)}$ [eV]	0.331	0.269	0.016
$\Omega^{(12)}$ [eV]	0.223	0.012	-0.194
$T_c^{(11)}$ [K]	~ 1980	~ 1600	~ 100
$T_c^{(12)}$ [K]	~ 1340	~ 70	0

itates void and pit formation. Interestingly, the (111) facet exhibits the opposite behavior: the intra-plane interactions, albeit attractive, are relatively weak, while the inter-plane ones are stronger, but highly repulsive. This suggests that, under equilibrium and at normal operating conditions, the (111) surface, by having perfect vacancy solubility, is the most likely to prevent the issue of void formation and pitting. The expected behavior of these surface is shown in Figure 2.

Note that, for all facets considered, vacancies on the same layer attract each other. However, these interactions are much stronger in the (100) and (110) cases, the two surfaces in which the distance between neighboring sites is closer to 3.5 Å, the lattice parameter of a conventional lithium unit cell. For the (111) facet, the large distance $\langle d^{(11)} \rangle$ between neighboring sites diminishes the effects of a vacancy on its neighbors, allowing entropy to dominate the Gibbs free energy at even low temperatures. This large distance also contributes to the relatively high atomic-level roughness of this facet when compared to its (100) and (110) counterparts, something that is reflected in the relative surface energies of

these facets. We believe that this partially contributes to the repulsive inter-layer interactions between vacancies: having neighboring vacancies in the two top layers would only increase said roughness.

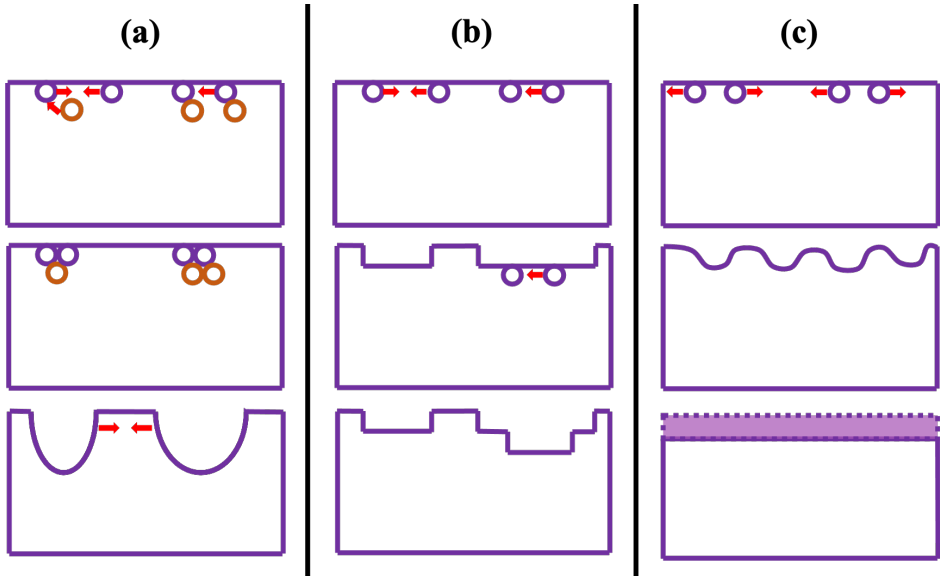


Figure 2: Side-view schematic of the expected behavior of **(a)** (100), **(b)** (110), and **(c)** (111) lithium surface facets during stripping. The removal of atoms during discharge creates vacancies on the surface, denoted by circles. Purple circles represent vacancies on the surface-level Miller plane, and orange circles are vacancies on the second outer-most layer. Red arrows show the interactions between vacancies. In the (100) facet, vacancies will attract each other regardless of layer, and can thus form large (in an atomistic scale) valleys. The (110) surface exhibits a somewhat similar behavior, but, due to the inter-layer vacancy repulsion, vacancies would only congregate on the surface-level Miller plane. By doing so, they form steps that expose the underlying layer and creates a new surface for lithium extraction. In this case, valleys would be formed as a collection of terraces. The (111) facet shows the most promise: the strong inter-layer vacancy repulsion, coupled with the weak intra-layer attraction, will force vacancies to be uniformly distributed on the surface. In doing so, when enough lithium is stripped, a relatively flat surface will emerge. The light pink rectangle in panel (c) enclosed by the dashed line indicates the stripped layer.

This work uses the regular solution model to examine vacancy congregation on different lithium metal surface facets, which constitutes the first step in the process of void formation and subsequent pitting that plagues lithium metal anodes. Our study identifies that the (111) surface facet could help mitigate this issue under equilibrium conditions. Kinetic effects can promote vacancy congregation in the (111) facet: if vacancies are created faster than they

can diffuse on the surface, voids, and eventually pits, will irrevocably form. This will be the subject of future investigations and will provide a deeper understanding of mechanism of void formation and pitting in lithium metal anodes. This fundamental mechanistic understanding developed here provides a rational basis for enabling fast-discharging lithium metal batteries for electric aircraft.

Acknowledgement

This work was supported in part by the Advanced Research Projects Agency-Energy Integration and Optimization of Novel Ion Conducting Solids (IONICS) program under Grant No. DEAR0000774. Acknowledgment is also made to the Extreme Science and Engineering Discovery Environment (XSEDE) for providing computational resources through Award No. TG-CTS180061.

Supporting Information Available

The following files are available free of charge.

- Li_stripping_surf_SI.pdf: Computational details of simulations and of parameter estimation for regular solution model.

References

- (1) Sun, Y.; Liu, N.; Cui, Y. Promises and challenges of nanomaterials for lithium-based rechargeable batteries. *Nat Energy* **2016**, *1*, 1–12.
- (2) Aurbach, D.; Zinigrad, E.; Teller, H.; Dan, P. Factors which limit the cycle life of rechargeable lithium (metal) batteries. *J Electrochem Soc* **2000**, *147*, 1274.

- (3) Lin, D.; Liu, Y.; Cui, Y. Reviving the lithium metal anode for high-energy batteries. *Nature Nano* **2017**, *12*, 194.
- (4) Sripad, S.; Viswanathan, V. Performance Metrics Required of Next-Generation Batteries to Make a Practical Electric Semi Truck. *ACS Energy Lett.* **2017**, *2*, 1669–1673.
- (5) Fredericks, W. L.; Sripad, S.; Bower, G. C.; Viswanathan, V. Performance Metrics Required of Next-Generation Batteries to Electrify Vertical Takeoff and Landing (VTOL) Aircraft. *ACS Energy Lett.* **2018**, *3*, 2989–2994.
- (6) Epstein, A. H.; O’Flarity, S. M. Considerations for Reducing Aviation’s CO₂ with Aircraft Electric Propulsion. *J. Propul. Power* **2019**, *35*, 572–582.
- (7) Bills, A.; Sripad, S.; Fredericks, W. L.; Guttenberg, M.; Charles, D.; Frank, E.; Viswanathan, V. Universal Battery Performance and Degradation Model for Electric Aircraft. *arXiv preprint [arXiv:2008.01527](https://arxiv.org/abs/2008.01527)* **2020**,
- (8) Xu, W.; Wang, J.; Ding, F.; Chen, X.; Nasybulin, E.; Zhang, Y.; Zhang, J.-G. Lithium metal anodes for rechargeable batteries. *Energy & Environ Sci* **2014**, *7*, 513–537.
- (9) Fu, C.; Venturi, V.; Kim, J.; Ahmad, Z.; Ells, A. W.; Viswanathan, V.; Helms, B. A. Universal chemomechanical design rules for solid-ion conductors to prevent dendrite formation in lithium metal batteries. *Nat Mater* **2020**, 1–9.
- (10) Bhowmik, A.; Castelli, I. E.; Garcia-Lastra, J. M.; Jørgensen, P. B.; Winther, O.; Vegge, T. A perspective on inverse design of battery interphases using multi-scale modelling, experiments and generative deep learning. *Energy Storage Mater* **2019**, *21*, 446–456.
- (11) Sharafi, A.; Kazyak, E.; Davis, A. L.; Yu, S.; Thompson, T.; Siegel, D. J.; Dasgupta, N. P.; Sakamoto, J. Surface chemistry mechanism of ultra-low interfacial resistance in the solid-state electrolyte Li₇La₃Zr₂O₁₂. *Chem Mater* **2017**, *29*, 7961–7968.

- (12) Exner, K. S. Constrained Ab Initio Thermodynamics: Transferring the Concept of Surface Pourbaix Diagrams in Electrocatalysis to Electrode Materials in Lithium-Ion Batteries. *ChemElectroChem* **2017**, *4*, 3231–3237.
- (13) Exner, K. S. A short perspective of modeling electrode materials in lithium-ion batteries by the ab initio atomistic thermodynamics approach. *J Solid State Electr* **2018**, *22*, 3111–3117.
- (14) Gialampouki, M. A.; Hashemi, J.; Peterson, A. A. The electrochemical mechanisms of solid–electrolyte interphase formation in lithium-based batteries. *J Phys Chem C* **2019**, *123*, 20084–20092.
- (15) Yan, K.; Lu, Z.; Lee, H.-W.; Xiong, F.; Hsu, P.-C.; Li, Y.; Zhao, J.; Chu, S.; Cui, Y. Selective deposition and stable encapsulation of lithium through heterogeneous seeded growth. *Nat Energy* **2016**, *1*, 1–8.
- (16) Li, W.; Yao, H.; Yan, K.; Zheng, G.; Liang, Z.; Chiang, Y.-M.; Cui, Y. The synergetic effect of lithium polysulfide and lithium nitrate to prevent lithium dendrite growth. *Nat Commun* **2015**, *6*, 1–8.
- (17) Lu, Y.; Tu, Z.; Archer, L. A. Stable lithium electrodeposition in liquid and nanoporous solid electrolytes. *Nat Mater* **2014**, *13*, 961–969.
- (18) Qian, J.; Henderson, W. A.; Xu, W.; Bhattacharya, P.; Engelhard, M.; Borodin, O.; Zhang, J.-G. High rate and stable cycling of lithium metal anode. *Nat Commun* **2015**, *6*, 1–9.
- (19) Zhang, J.-G.; Xu, W.; Henderson, W. A. *Lithium metal anodes and rechargeable lithium metal batteries*; Springer International Publishing (Basel, Switzerland), 2017.
- (20) Zhao, J.; Liao, L.; Shi, F.; Lei, T.; Chen, G.; Pei, A.; Sun, J.; Yan, K.; Zhou, G.; Xie, J.,

- et al. Surface fluorination of reactive battery anode materials for enhanced stability. *J Am Chem Soc* **2017**, *139*, 11550–11558.
- (21) Hatzell, K. B.; Chen, X. C.; Cobb, C. L.; Dasgupta, N. P.; Dixit, M. B.; Marbella, L. E.; McDowell, M. T.; Mukherjee, P. P.; Verma, A.; Viswanathan, V., et al. Challenges in lithium metal anodes for solid-state batteries. *ACS Energy Lett* **2020**, *5*, 922–934.
- (22) Jäckle, M.; Helmbrecht, K.; Smits, M.; Stottmeister, D.; Groß, A. Self-diffusion barriers: possible descriptors for dendrite growth in batteries? *Energy Environ Sci* **2018**, *11*, 3400–3407.
- (23) Jäckle, M.; Groß, A. Microscopic properties of lithium, sodium, and magnesium battery anode materials related to possible dendrite growth. *J Chem Phys* **2014**, *141*, 174710.
- (24) Wang, M. J.; Choudhury, R.; Sakamoto, J. Characterizing the Li-solid-electrolyte interface dynamics as a function of stack pressure and current density. *Joule* **2019**, *3*, 2165–2178.
- (25) Wood, K. N.; Kazyak, E.; Chadwick, A. F.; Chen, K.-H.; Zhang, J.-G.; Thornton, K.; Dasgupta, N. P. Dendrites and pits: Untangling the complex behavior of lithium metal anodes through operando video microscopy. *ACS Cent Sci* **2016**, *2*, 790–801.
- (26) Cohen, Y. S.; Cohen, Y.; Aurbach, D. Micromorphological studies of lithium electrodes in alkyl carbonate solutions using in situ atomic force microscopy. *J Phys Chem B* **2000**, *104*, 12282–12291.
- (27) Shi, F.; Pei, A.; Boyle, D. T.; Xie, J.; Yu, X.; Zhang, X.; Cui, Y. Lithium metal stripping beneath the solid electrolyte interphase. *Proc Natl Acad Sci U S A* **2018**, *115*, 8529–8534.
- (28) Gireaud, L.; Grugeon, S.; Laruelle, S.; Yrieix, B.; Tarascon, J.-M. Lithium metal strip-

- ping/plating mechanisms studies: A metallurgical approach. *Electrochem Commun* **2006**, *8*, 1639–1649.
- (29) Monroe, C.; Newman, J. The impact of elastic deformation on deposition kinetics at lithium/polymer interfaces. *J Electrochem Soc* **2005**, *152*, A396.
- (30) Ahmad, Z.; Viswanathan, V. Stability of electrodeposition at solid-solid interfaces and implications for metal anodes. *Phys Rev Lett* **2017**, *119*, 056003.
- (31) Kasemchainan, J.; Zekoll, S.; Spencer Jolly, D.; Ning, Z.; Hartley, G. O.; Marrow, J.; Bruce, P. G. Critical stripping current leads to dendrite formation on plating in lithium anode solid electrolyte cells. *Nat Mater* **2019**, *18*, 1105–1111.
- (32) Perdew, J. P.; Burke, K.; Ernzerhof, M. Generalized Gradient Approximation Made Simple. *Phys Rev Lett* **1996**, *77*, 3865–3868.
- (33) Enkovaara, J.; Rostgaard, C.; Mortensen, J. J.; Chen, J.; Dułak, M.; Ferrighi, L.; Gavnholt, J.; Glinzvad, C.; Haikola, V.; Hansen, H., et al. Electronic structure calculations with GPAW: a real-space implementation of the projector augmented-wave method. *J Phys: Condens Matter* **2010**, *22*, 253202.
- (34) Larsen, A. H.; Mortensen, J. J.; Blomqvist, J.; Castelli, I. E.; Christensen, R.; Dułak, M.; Friis, J.; Groves, M. N.; Hammer, B.; Hargus, C., et al. The atomic simulation environment—a Python library for working with atoms. *J Phys: Condens Matter* **2017**, *29*, 273002.
- (35) Shi, F.; Pei, A.; Vailionis, A.; Xie, J.; Liu, B.; Zhao, J.; Gong, Y.; Cui, Y. Strong texturing of lithium metal in batteries. *Proc Natl Acad Sci U S A* **2017**, *114*, 12138–12143.

Supporting Information: Thermodynamics of Lithium Stripping and Limits for Fast Discharge in Lithium Metal Batteries

Victor Venturi[†] and Venkatasubramanian Viswanathan^{*,†,‡}

*†Department of Mechanical Engineering, Carnegie Mellon University, Pittsburgh,
Pennsylvania 15213, USA*

‡Department of Physics, Carnegie Mellon University, Pittsburgh, Pennsylvania 15213, USA

E-mail: venkvis@cmu.edu

Computational details of interaction parameter estimation

In order to estimate the different regular solution parameters needed for our modeling, we used density functional theory (DFT), coupled with the Perdew, Burke, and Ernzerhof (PBE) exchange correlation functional¹ in the projector augmented wave (PAW) code GPAW.² The structures used were all slabs of at least 4 layers, with the bottom 2 layers kept fixed as to emulate bulk lithium, and can be seen in Figure S1. A 10 Å vacuum was applied, alongside a real-space grid spacing of 0.16 Å and a Monkhorst Pack scheme³ sampling of the Brillouin zone with k-point density of 6 Å⁻¹. All calculations were converged to energy < 0.5 meV and force < 0.05 eV·Å⁻¹.

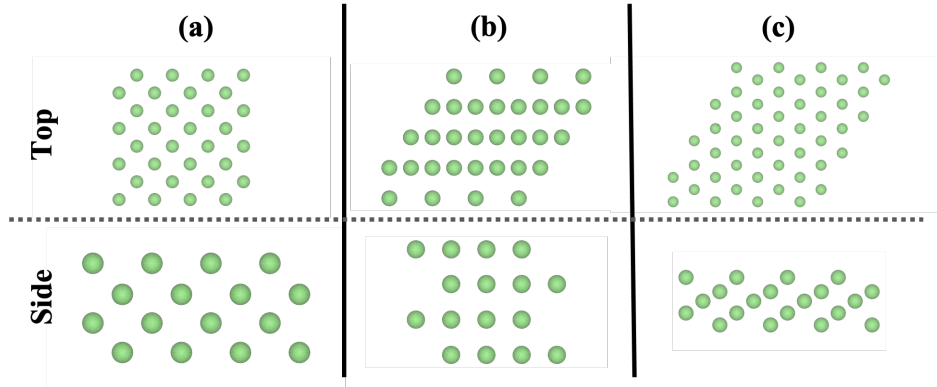


Figure S1: Top and side views of the structures used to calculate interaction parameters for the (a) (100), (b) (110), and (c) (111) surface facets. All structures had a minimum of 4 layers, and the bottom two layers of each structures were kept fixed to properly emulate bulk lithium.

To estimate the interaction parameters, systems with only one vacancy were created, allowing us to evaluate, for each facet, the value of $\epsilon_{VL} - \epsilon_{LL}$: the difference in energy between the pristine system and that with a vacancy is given by $E_{\text{single vacancy}} - E_{\text{pristine}} = z(\epsilon_{VL} - \epsilon_{LL})$. Next, by incorporating a second vacancy neighboring the first one, the value of $\epsilon_{VV} - \epsilon_{LL}$ can be estimated: $E_{\text{two vacancies}} - E_{\text{pristine}} = 2(z - 1)(\epsilon_{VL} - \epsilon_{LL}) + (\epsilon_{VV} - \epsilon_{LL})$. Finally, to calculate the full interaction parameter we use

$$\Omega = \frac{z}{2} [2(\epsilon_{VL} - \epsilon_{LL}) - (\epsilon_{VV} - \epsilon_{LL})] = \frac{z}{2} (2\epsilon_{VL} - \epsilon_{VV} - \epsilon_{LL})$$

References

- (1) Perdew, J. P.; Burke, K.; Ernzerhof, M. Generalized Gradient Approximation Made Simple. *Phys Rev Lett* **1996**, *77*, 3865–3868, DOI: 10.1103/PhysRevLett.77.3865.
- (2) Enkovaara, J.; Rostgaard, C.; Mortensen, J. J.; Chen, J.; Dułak, M.; Ferrighi, L.; Gavnholt, J.; Glinsvad, C.; Haikola, V.; Hansen, H., et al. Electronic structure calculations with GPAW: a real-space implementation of the projector augmented-wave method. *J Phys: Condens Matter* **2010**, *22*, 253202, DOI: 10.1088/0953-8984/22/25/253202.
- (3) Monkhorst, H. J.; Pack, J. D. Special points for Brillouin-zone integrations. *Physical review B* **1976**, *13*, 5188.

Graphical TOC Entry

